Check for updates

Interfacial interactions of doped-Ti₃C₂ MXene/MAPbI₃ heterostructures: surfaces and the theoretical approach†

Muhammad Abiyyu Kenichi Purbayanto, [ID] [a] Arramel, [ID] *[b] See Wee Koh, [cd] Francesco Maddalena, [ID] [d] Dorota Moszczyńska, [a] Jessie Manopo, [ID] [e] Yudi Darma, [ID] *[ef] Dominik Kowal, [ID] [g] Hong Li, [ID] [cd] Muhammad Danang Birowosuto [ID] *[g] and Agnieszka Maria Jastrzębska [ID] *[a]

The work function (WF) of perovskite materials is essential for developing optoelectronic devices enabling efficient charge transfer at their interfaces. Perovskite's WF can be tuned by MXenes, a new class of two-dimensional (2D) early transition metal carbides, nitrides, and carbonitrides. Their variable surface terminations or the possibility of introducing elemental dopants could advance perovskites. However, the influence of doped-MXenes on perovskite materials is still not fully understood and elaborated. This study provides mechanistic insight into verifying the tunability of MAPbI₃ WF by hybridizing with fluorine-terminated Ti₃C₂Tₓ (F-MXene) and nitrogen-doped Ti₃C₂Tₓ (N-MXene). We first reveal the interfacial interaction between MAPbI₃ and MXenes *via* X-ray photoelectron spectroscopy (XPS), ultraviolet photoelectron spectroscopy (UPS), and photoluminescence spectroscopy (PL). UPS supported by density functional theory (DFT) calculations allowed the description of the influence of F and N on MXene's WF. Furthermore, we developed MAPbI₃/MXene heterostructures using F- and N-MXenes. The F-MXenes extended the most WF of MAPbI₃ from 4.50 eV up to 3.00 eV, compared to only a small shift for N-MXene. The underlying mechanism was charge transfer from low WF F-MXene to MAPbI₃, as demonstrated by PL quenching in MAPbI₃/F-MXene heterostructures. Altogether, this work showcases the potential of fluorine-doped MXenes over nitrogen-doped MXenes in advancing perovskite heterostructures, thus opening a door for efficient optoelectronic devices.

1. Introduction

Hybrid organic–inorganic perovskites are promising materials for applications in photovoltaic devices due to their high efficiency, low fabrication cost, bandgap tunability, and excellent optical absorption.[1] One of their critical parameters is the work function (WF). Perovskite's WF is an essential parameter for tuning band alignment and charge transfer at materials interfaces, realizing a high photovoltaic device performance.[2] Notably, WF can be tuned by two-dimensional (2D) materials such as MXenes.

MXenes are a novel family of 2D materials called early transition metal carbides, nitrides, and carbonitrides. They are represented by the $M_{n+1}X_nT_x$ (n = 1–4) chemical formula,

[a] Faculty of Materials Science and Engineering, Warsaw University of Technology, Wołoska 141, 02-507 Warsaw, Poland. E-mail: agnieszka.jastrzebska@pw.edu.pl

[b] Nano Center Indonesia, Jalan Raya PUSPIPTEK, South Tangerang, Banten 15314, Indonesia. E-mail: arramel@nano.or.id

[c] School of Mechanical and Aerospace Engineering, Nanyang Technological University, 639798, Singapore

[d] CINTRA CNRS/NTU/THALES, UMI 3288, Research Techno Plaza, 637553, Singapore

[e] Department of Physics, Institut Teknologi Bandung, Jalan Ganesa No. 10, Bandung 40132, Indonesia. E-mail: yudi@itb.ac.id

[f] Research Collaboration Center for Quantum Technology 2.0, Bandung 40132, Indonesia

[g] Łukasiewicz Research Network—PORT Polish Center for Technology Development, Stabłowicka 147, 54-066 Wrocław, Poland.
  E-mail: muhammad.birowosuto@port.lukasiewicz.gov.pl

† Electronic supplementary information (ESI) available: Figures: SEM images of F-MXene and N-MXene; EDS of F-MXene; XPS survey spectra of N-MXene and F-MXene; XPS spectra of F-MXene, N-MXene, and the MAPbI₃/MXene heterostructure; EDS mapping of the F-MXene/MAPbI₃ heterostructure; plane averaged electrostatic potential *vs.* z for F-MXene, N-MXene, and –OH terminated MXene; PDOS and DOS of –OH terminated MXene, F-terminated MXene, and N-doped MXene; ELF of F-MXene FCC and N-MXene HCP; SECO signals of MAPbI₃. Tables: chemical composition of as-synthesized MXene obtained from EDS; relative formation energy for every adsorption site of F- and N-MXene; summary of MXene WF obtained from experiment and DFT prediction; and summary of WF and VB changes in MXene/MAPbI₃ heterostructures. See DOI: https://doi.org/10.1039/d3cp04018f

This journal is © the Owner Societies 2023

Phys. Chem. Chem. Phys., 2023, **25**, 33081–33093 | **33081**

in which M is a transition metal, and X denotes carbon or nitrogen. T_x refers to functional groups present on MXene surfaces, such as O, OH, and F,[3] making MXenes highly dispersible in water and suitable for solution processing methods.[4] MXenes exhibit remarkable physical properties, such as outstanding electrical conductivity ($> 2.0 \times 10^4$ S cm^{-1}),[5] high carrier density (3.8×10^{22} cm^{-3}),[6] and exceptional carrier mobility (1 cm^2 V^{-1} s^{-1}).[6] MXene's optoelectronic properties become even more attractive due to their tunability. For instance, MXene's band structure can be altered by changing the transition metal's chemical structure or modifying the surface *via* functionalization.[7]

Introducing different surface terminations can control the WF of $Ti_3C_2T_x$ MXene.[8,9] These experimental findings were confirmed through density functional theory (DFT) calculations, which predicted that the WF of $Ti_3C_2T_x$ MXene spans a broad energy range from 1.6 eV (–OH termination) to 6.25 eV (–O termination).[10,11] Agresti *et al.* demonstrated the tunability of perovskite's WF by introducing MXene surface-terminated with –F, –OH, and –O functional groups.[12] Incorporating the $Ti_3C_2(OH)_2$ MXene reduced WF of MAPbI$_3$ from 4.72 eV to 4.37 eV. The decrease of WF was induced by the dipole interaction and band alignment at the vicinity of the MAPbI$_3$/$Ti_3C_2(OH)_2$ interface, while the power conversion efficiency of MXene-modified perovskite reached 26%.[12] Given the importance of tuneable WF in device fabrication, this behaviour is particularly promising when combined in a heterostructure assembly. WF tuning plays an essential role in the development of optoelectronic devices. The palette of approaches includes improving the charge transfer capability, constructing Schottky barriers, and determining the catalytic surface activity.[13,14]

MXenes have also been utilised as functional building blocks for optically active heterostructures.[15–18] MXene-based heterostructures were developed for various applications, including photocatalysts,[15] photodetectors,[16] and photovoltaics.[19] For instance, adding $Ti_3C_2T_x$ to MAPbI$_3$ facilitates more efficient electron transfer through the grain boundary.[20] Furthermore, several researchers demonstrated other advantages of coupling $Ti_3C_2T_x$ MXene with perovskites, such as robust optical absorption,[21] WF alignment,[12] controlled nucleation and crystallization of perovskites,[19] and their efficient charge carrier transportation.[22]

Elemental doping of MXenes with non-metallic elements could enhance electrical conductivity, providing excellent WF tunability.[23,24] However, an interplay between doped-MXene and perovskite in terms of the electronic structure and WF tuning is still not fully understood, although non-metallic doped MXenes already showed promising results in various opto- and electrochemical properties. For instance, by introducing nitrogen doping into $Ti_3C_2T_x$ MXene lattices, the electrical conductivity and electron concentration of $Ti_3C_2T_x$ can be increased compared with pristine $Ti_3C_2T_x$.[25] Furthermore, nitrogen-doped $Ti_3C_2T_x$ displayed a remarkable performance as an electrode for supercapacitor applications. An improvement of specific capacitance of 460% compared to the pristine led to excellent cyclic stability after 10 000 charge and discharge cycles.[25,26] In microwave absorbing applications, nitrogen

doping can be a suitable alternative for magnetic nanoparticle fillers in $Ti_3C_2T_x$, which are susceptible to oxidation even at room temperature (RT).[27]

However, mechanisms responsible for the interaction between surface-terminated or doped MXenes and perovskites are still not fully understood, especially in their influence on perovskite's electronic structure and WF. Hence, in this study, we aim to investigate the effect of fluorine termination and nitrogen doping of $Ti_3C_2T_x$ on interfacial interactions with MAPbI$_3$ perovskite. We have synthesized F-terminated $Ti_3C_2T_x$ *via* conventional HF etching while N-doped $Ti_3C_2T_x$ through thermal annealing. We further deposited MAPbI$_3$ on MXene surfaces *via* a spin-coating technique and verified their optoelectronic properties and WF for F-MXene/MAPbI$_3$ and N-MXene/MAPbI$_3$ heterostructures.

Results from ultraviolet photoelectron spectroscopy (UPS), X-ray photoelectron spectroscopy (XPS), and photoluminescence spectroscopy (PL) showed that F-termination and N-doping significantly alter the WF of MAPbI$_3$. MXenes effectively tuned the band alignment and interfacial charge transfer in MXene/perovskite heterostructures, which could enhance the optoelectronic device performance. Additionally, performed DFT calculations further supported our experimental findings.

This work demonstrates the potential of non-metal element additives to MXenes as a promising approach for developing high-performance MXene/perovskite heterostructures. Our study provides new insight into the heterostructure design of perovskite-based optoelectronic devices.

2. Materials and methods

2.1. Synthesis of $Ti_3C_2T_x$ MXene

$Ti_3C_2T_x$ MXene was synthesized by selective etching of the Ti_3AlC_2 MAX phase (Y-carbon Ukraine) with 48 wt% water solution of hydrofluoric acid (Sigma Aldrich, 695068). The 5-day etching process ensured complete etching out of aluminium and allowed high fluorine saturation of the MXene surface. After etching, MXene flakes were washed with distilled water (6000 rpm for 20 min) until the pH reached around 6. Then, MXene was dried overnight in a vacuum oven at 60 °C.

2.2. Synthesis of F-terminated and N-doped MXene

In order to delaminate MXene, previously etched MXene powders with high fluorine saturation (0.3 grams) were sonicated in methanol for 60 min. Next, the delaminated MXene was centrifuged at 3500 rpm for 10 min to separate MXene from methanol. The sediment was further dried to collect MXene powders. As the MXene powders were highly functionalized by fluorine, we called it F-MXene in the entire paper. The dried MXene was then separated into different alumina crucibles for use in a tube furnace. Nitrogen-doped MXene (N-MXene) was acquired *via* thermal annealing 100 mg of as-etched MXene at 200 °C for 7 hours under a constant flow (10 sccm) of 10% ammonia in argon (10% NH$_3$: 90% Ar, Air Products). Au on Si and Si/SiO$_2$ substrates were used to compare the physicochemical properties

33082 | *Phys. Chem. Chem. Phys.,* 2023, **25**, 33081–33093

This journal is © the Owner Societies 2023

of MXene in different electronic environments. The powders of F-MXene and N-MXene were further dispersed in methanol and drop-casted on 100 nm-thick Au on Si or Si/SiO_2 substrates.

2.3. MAPbI$_3$ thin film fabrication

Perovskite thin films were deposited on previously prepared MXene on the top of 100 nm-thick Au on Si or Si/SiO_2 substrates. Hereafter, the prepared films were denoted as the MAPbI$_3$/MXene heterostructure. The perovskite solution was prepared by dissolving MAI and PbI$_2$ with a molar ratio of 1:1 in *N,N*-dimethylformamide (DMF) (0.5 M) and stirred at 100 °C until complete dissolution. The MAPbI$_3$ thin film was prepared by spin-casting a precursor solution on the top of MXene samples at 2000 rpm (acceleration = 500 rpm) for 30 s and blow-drying with N$_2$ during the last 15 s when the sample was spinning, giving a thickness of ~500 nm. The thin film was then placed on the surface of a hot plate and annealed at 100 °C for 15 min. MAPbI$_3$ was relatively stable within humidity and the sample could withstand ~1 week in the open air. However, the measurement was performed using the as-received sample (same day) to avoid damaging the samples.

2.4. Morphology and structural characterization

The as-prepared Ti$_3$C$_2$T$_x$ (F-MXene) powder morphology was characterized using field-emission scanning electron microscopy (FESEM) of Hitachi S5500, Japan. Moreover, the morphology of F-MXene and N-MXene thin films was characterized using FESEM JEOL JSM-7600F, Japan. The micrographs were taken at an accelerating voltage of 6 kV in the secondary electron mode. The crystal structures of the Ti$_3$AlC$_2$ MAX phase and Ti$_3$C$_2$T$_x$ were studied using a Bruker D8-Advance X-ray diffractometer (Cu Kα −0.154056 nm). The entire experiment was carried out at RT.

2.5. XPS and UPS measurements

XPS experiments were carried out using an X-ray source of Magnesium Kα with a typical excitation energy output of 1254 eV. The XPS spectra were fitted using the Shirley background. UPS measurements were performed using a VG ESCA Lab system, an ultrahigh vacuum (UHV) system with a typical base pressure in the range of ~10^{-10} mbar equipped with a gas discharge lamp in which helium gas was passed into the analysis chamber. The UV source was an unfiltered He Iα (21.2 eV) excitation, and the sample was biased at −5 V to extract the low-energy secondary electron cut-off (SECO). The UV light spot size on the sample is about 1 mm in diameter. All the reported photoemission spectra were calibrated by referencing the Ag 3d$_{5/2}$ peak position (centered at 368.10 eV) of silver polycrystalline foil cleaned by standard argon ion sputtering treatment. The errors of all given values of binding energies and SECO positions are estimated to be ±0.05 eV.

2.6. Steady state and dynamic PL measurements

We used a standard micro-PL setup at RT using free-space excitation.[28] The samples were excited with a picosecond-pulsed ytterbium fiber laser emitting at 266 ± 2 nm and 532 ± 2 nm wavelength with a repetition rate of 10 MHz. The emission was observed through a 0.65-numerical-aperture visible-near-infrared microscope objective, by which the beam diameter was estimated to be 1 μm. PL spectra were recorded using an AvaSpec-HSC1024x 58TEC-EVO spectrometer. Time-resolved (TR-) PL measurements were carried out using single-photon counting detector modules from Micro Photon Devices connected to the single-photon counting acquisition module (TCC900, Edinburgh Instruments). We filtered the emission with a bandpass filter at 450 ± 25 nm or a long pass filter at 650 nm.

2.7. Computational methods

Theoretical calculations were carried out using the Quantum ESPRESSO (QE) package.[29] We employed an exchange–correlation functional developed by Perdew–Zunger[30] and the scalar-relativistic ultrasoft pseudopotential. The pseudopotential was chosen similar to the previous calculation.[12] We used a Monkhorst–Pack *k*-point mesh of 7 × 7 × 1 and a plane wave basis set cutoff of 60 Ry based on our optimization, as shown in Fig. S1 (ESI†). About ~10 Å vacuum was added within all calculations to the MXene structure to avoid the interaction with its image in the *z*-direction. The F and N surface terminations were added according to the previous report.[8] The work functions were calculated from the electrostatic potential calculated using the pp.*x* code in QE. The obtained electrostatic potential was further averaged in the *z* direction using the average from the *x* code in QE to obtain the work function.

We further performed N-doped Ti$_3$C$_2$T$_x$ MXene calculation using a 3 × 3 × 1 supercell, where one of the carbon atoms was replaced by a nitrogen atom. The adsorption sites of –F and –OH were chosen to be face-centred cubic (FCC) and hexagonal closed-packed (HCP), respectively, owing to the most energetically favourable configurations.

3. Results and discussion

MXene nanoflakes were prepared by etching the parental Ti$_3$AlC$_2$ MAX phase in 48 wt% aqueous HF solution. In this study, the etching process was done for five days to ensure the fluorine species fully terminated MXene. The synthesized F-MXene showed characteristic few-to-multilayered flakes (Fig. 1(a)) with a typical accordion-like open structure (Fig. S2, ESI†).[31,32] The X-ray diffraction pattern confirmed the successful preparation of Ti$_3$C$_2$T$_x$ MXene (F-MXene), as evidenced by broader XRD peaks and the absence of the corresponding Ti$_3$AlC$_2$ patterns (Fig. 1(b)).[33] Additionally, no diffraction patterns of TiO$_2$ were observed, implying the high quality of synthesized Ti$_3$C$_2$T$_x$ MXenes. Energy dispersive X-ray spectroscopy (EDS) analysis showed the presence of Ti, C, F, and O elements, with a negligible amount of Al (Fig. S3, ESI†). Interestingly, we obtained a high amount of F elements, suggesting dominant F-termination on the F-MXene surface, as we hypothesized before (Table S1, ESI†). After performing the nitrogen doping process, the surface morphology of MXene remains intact, as shown in Fig. S4 (ESI†).

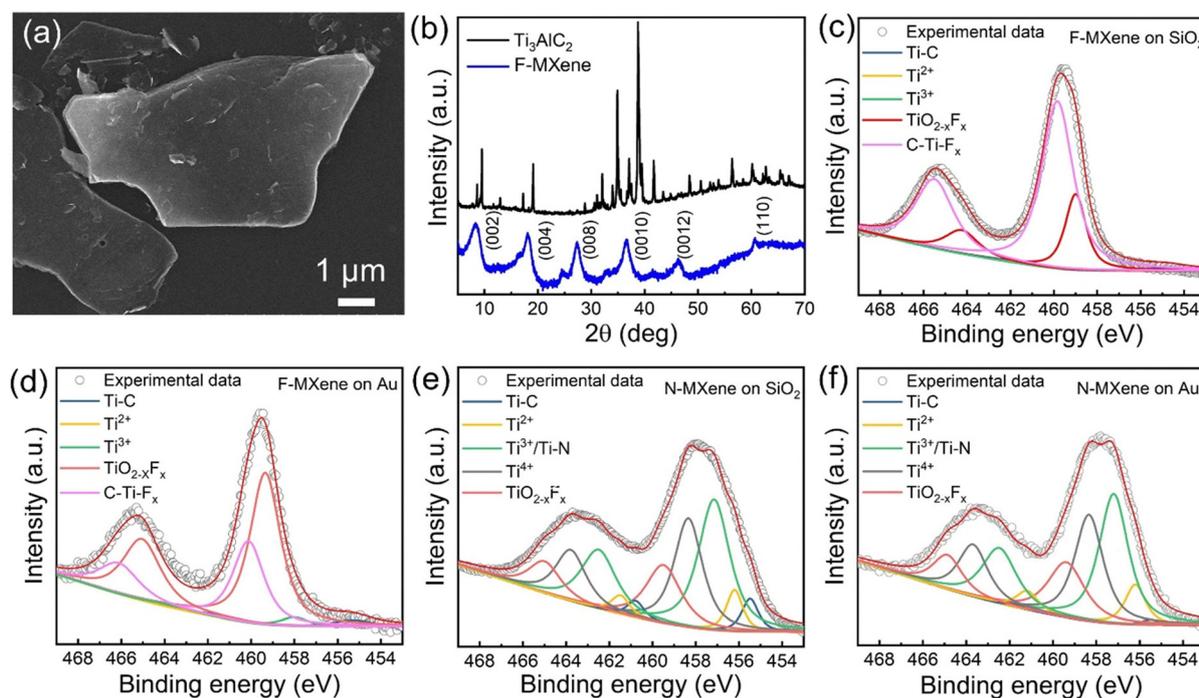This journal is © the Owner Societies 2023

Phys. Chem. Chem. Phys., 2023, **25**, 33081–33093 | **33083**

Fig. 1 (a) Scanning electron microscopy (SEM) images of as-synthesized F-MXene. (b) X-ray diffractogram of the Ti_3AlC_2 MAX phase and as-synthesized F-MXene. Ti 2p fitted X-ray photoelectron spectroscopy (XPS) components of (c) F-MXene on SiO_2, (d) F-MXene on Au, (e) N-MXene on SiO_2, and (f) N-MXene on Au.

We further conducted XPS analysis to study the chemical composition of F-MXene and N-MXene drop-casted on SiO_2 and Au substrates. XPS survey spectra (Fig. S5, ESI†) revealed the presence of Ti, C, and O in both F-MXene and N-MXene. In addition, F-MXene exhibited a strong fluorine signal, indicating successful fluorine surface termination, which aligns with EDS results. We detected the presence of nitrogen in the XPS survey spectra of N-MXene, indicating the successful introduction of nitrogen doping. In addition, we analysed each of the XPS survey spectra of the samples in a similar route as outlined by Deeva et al.[34] The elemental quantification of the F (N) to metal ratio of the respective samples are presented in Fig. S6 (ESI†). By comparing the area of F 1s and Ti 2p peaks, we unravel that the F/Ti ratio yields a high concentration of ca. 1.49 when the as-prepared F-MXenes were introduced onto the Au substrate. Our analysis here is in agreement with the previous report by Halim et al.[35] strengthening the fact that F has the dominant fraction of termination groups for Ti-based MXenes. Interestingly, a reasonable concentration (0.42) was achieved when these doped-MXenes were deposited onto SiO_2. In the case of N-MXene samples, we find a slightly reduced N/Ti ratio (0.17) on SiO_2 and (0.18) on Au. Based on this recent investigation, each of the T_x surface group functionalization in $Ti_3C_2T_x$ samples shows a contrasting atomic concentration profile of F(or N) species with respect to its metal constituent (Ti). The information regarding the ratio between F (N) and Ti could be further utilised to model MXene terminated locally by F or N. We envision that this will give a more precise local dipole distribution and detailed analysis of

the T_x species role as demonstrated by Schultz et al.[8] and Gouveia et al.[36]

The fitted Ti 2p XPS peaks of F-MXene deposited on SiO_2 (Fig. 1(c)) and Au (Fig. 1(d)) showed the presence of diverse Ti components, including Ti–C (455.3 eV), Ti^{2+} (456.3 eV), Ti^{3+} (458 eV), $TiO_{2-x}F_x$ (459.35 eV), and C–Ti–F_x (460.12 eV).[35,37] In this regard, the fluorine-related species, i.e., $TiO_{2-x}F_x$ and C–Ti–F_x, are observed to be present in substantial amounts. It is important to note that the value of the oxide component in F-MXene is located at a higher binding energy than pure TiO_2 oxides ($\sim$458.6 eV), indicating that the formed TiO_2 is majorly doped/terminated with F atoms.[37] This finding is reasonable as the HF etching process was performed for 5 days, resulting in high –F coverage on the surface of $Ti_3C_2T_x$.

In the case of N-MXene, nitrogen doping causes a redshift of the Ti 2p spectra. The redshifting suggests that the chemical environment of N-MXene differs from that of F-MXene. The fitted Ti 2p XPS spectra of N-MXene on SiO_2 and Au are presented in Fig. 1(e) and (f), respectively. Ti 2p XPS spectra of N-MXene can be fitted into five different components, consisting of Ti–C (455.48 eV), Ti^{2+} (456.2 eV), Ti^{3+}/Ti–N (457.15 eV), TiO_2 (458.34 eV), and $TiO_{2-x}F_x$ (459.49 eV).[23] In contrast to F-MXene, N-MXene showed a significant contribution of Ti^{3+}/Ti–N, implying that nitrogen atoms substitute titanium atoms in the MXene crystal lattice.[23] These findings suggest that the chemical composition and oxidation states of MXene can be effectively tuned through doping, which can significantly impact various applications, including optoelectronic devices.

33084 | Phys. Chem. Chem. Phys., 2023, **25**, 33081–33093

This journal is © the Owner Societies 2023

Fig. S7 (ESI†) presents the O 1s XPS spectra of F-MXene and N-MXene, providing insight into the functional groups on the respective surfaces. For F-MXene, the spectra show the contribution from TiO_2 (529.8 eV), $C–Ti–O_x$ (531.7 eV), and $C–Ti–(OH)_x$ (532.7 eV). Therefore, the XPS core levels of O 1s and Ti 2p confirm that F-MXene is successfully functionalized with the mix of –F, –OH, and –O functional groups. On the other hand, O 1s XPS spectra of N-MXene are fitted by TiO_2 (529.8 eV), $C–Ti–(OH)_x$ (532.3 eV), and N–O (534.5 eV). In contrast to F-MXene, N-MXene is majorly terminated by the –OH functional group. Additionally, N–O suggests partial nitrogen incorporation within the surface functional groups.[38] Nonetheless, we also observe a minor contribution of the –F functional group on N-MXene, which we will discuss further through XPS F 1s analysis.

Fig. S8 (ESI†) shows the F 1s XPS spectra of F-MXene and N-MXene. Here, F-MXene spectra can be fitted into three components, including $C–Ti–F_x$ (684.6 eV), $TiO_{2−x}F_x$ (685.2 eV), and AlF_x (686.2 eV). The presence of the AlF_x component is attributed to the by-product generated during the etching process.[35] On the other hand, N-MXene spectra show two components, namely $C–Ti–F_x$ (684.1 eV) and $Al(OF)_x$ (688.3 eV), with the latter originating from the synthesised by-product. Moreover, we emphasize that the –F terminated related species account for only a small fraction of N-MXene. In contrast, F-MXene exhibits a high amount of –F terminated $Ti_3C_2T_x$, indicating the rich surface fluorine (–F) termination on the MXene surface.

To further explore the nature of nitrogen doping in N-MXene, we move to the N 1s core level of XPS spectra. The fitted N 1s XPS spectra of N-MXene (Fig. S9, ESI†) exhibit a significant contribution from Ti–N (396.5 eV),[39] with a minor contribution from O–Ti–N (397.3 eV)[40] components. The presence of Ti–N in both Ti 2p and N 1s XPS spectra confirms the successful lattice substitution of C atoms with N atoms in the $Ti_3C_2T_x$ structure.[25,38] Furthermore, O–Ti–N can be connected to the decoration of nitrogen on the surface functional groups. Therefore, in our study, in addition to nitrogen substituting carbon atoms, as indicated by the Ti–N component, nitrogen also decorated the MXene surface, as demonstrated by the O–Ti–N XPS component.

Following the successful synthesis of F-MXene and N-MXene, we fabricated the $MAPbI_3$/MXene heterostructure. To achieve this, thin film layers of MXene and $MAPbI_3$ were prepared on SiO_2 and the Au substrate using the spin-coating technique. Fig. 2(a) provides a schematic illustration of the fabrication process of the $MAPBI_3$/MXene heterostructure. In particular, $MAPbI_3$ layers were spin-coated on as-fabricated MXene layers. The heterostructured films show similar thicknesses (around 2 μm) as measured in MXene and $MAPbI_3$ alone. This observation could be attributed to the consistency of the films obtained from the MXene drop-casting process and the deposited films' relatively thick nature. Tilted SEM images of F-MXene, $MAPbI_3$, and $MAPbI_3$/MXene thin films deposited on the SiO_2 substrate are displayed in Fig. 2(b)–(e). The SEM images confirm that the perovskite film well penetrated into MXene layers. Interestingly, upon $MAPbI_3$ deposition on the MXene surface, the morphology of the thin film shows a smooth layer. This is attributed to the role of functional groups on the MXene surface in ensuring uniform blending between MXene and perovskite without introducing any aggregation. Furthermore, the EDS mapping of the heterostructured film (Fig. S10, ESI†) confirmed the presence of both $Ti_3C_2T_x$ and $MAPbI_3$.

We further performed XPS measurements to probe the chemical composition of the $MAPbI_3$/MXene heterostructured thin film. XPS spectra of $MAPbI_3$/N-MXene and $MAPbI_3$/F-MXene
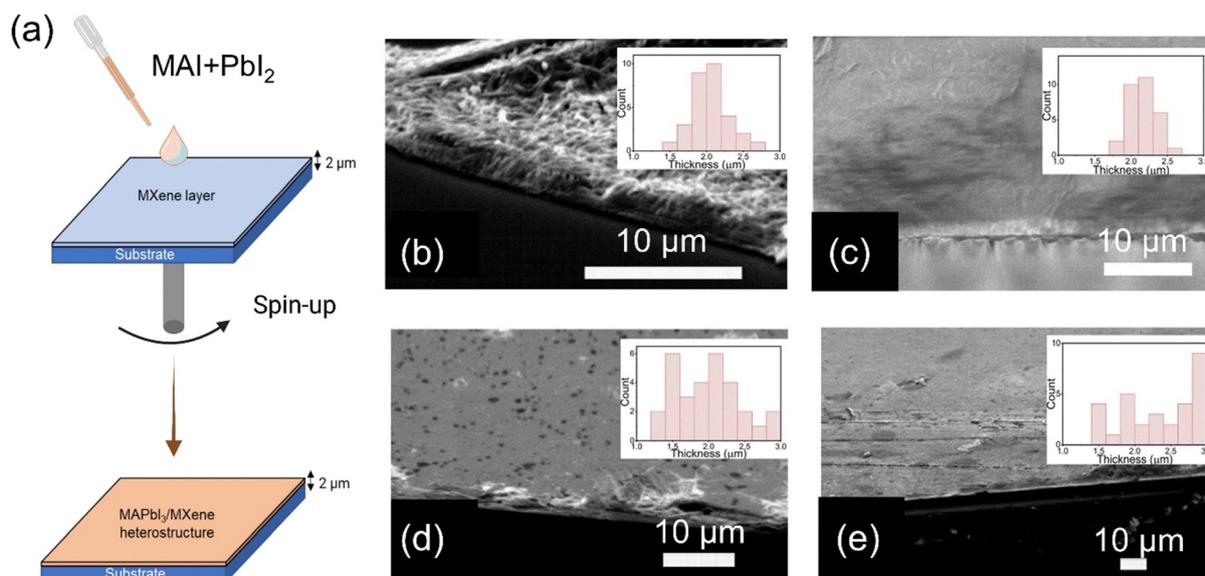

Fig. 2 (a) Schematic diagram of the $MAPbI_3$/MXene heterostructure fabrication procedure. Tilted cross-sectional SEM images of (b) F-MXene, (c) $MAPbI_3$, (d) N-MXene/$MAPbI_3$, and (e) F-MXene/$MAPbI_3$ thin films deposited on the SiO_2/Si substrate. The inset shows the thickness distribution of the films. All thicknesses are about 2 μm, indicating perovskite layers were well penetrated to the MXene structure.

This journal is © the Owner Societies 2023

Phys. Chem. Chem. Phys., 2023, 25, 33081–33093 | 33085

grown on SiO$_2$ and Au substrates are presented in Fig. S11–S14 (ESI†). All the samples show C 1s, N 1s, O 1s, Ti 2p, Pb 4f, and I 3d XPS signals. Pb 4f shows symmetrical doublet peaks corresponding to the spin–orbit splitting of Pb 4f$_{7/2}$ and 4f$_{5/2}$ components from the Pb^{2+} cation in the MAPbI$_3$ crystal structure.[41] We do not observe any Pb 4f components located at a lower binding energy, indicating that no metallic Pb is formed during the perovskite preparation.[42] Furthermore, the I 3d core level shows a single doublet peak, originating from 3d$_{5/2}$ and 3d$_{3/2}$, showing that only a single I component was observed in the film. Besides the contribution of I 3d and Pb 4f signals, we also observe the N 1s core level, which is related to the MA$^+$ of the MAPbI$_3$ structure.[43] As MAPbI$_3$ is deposited on the surface of MXene, the absence of the Ti 2p signal suggests that MAPbI$_3$ effectively covers the MXene surface. Thus, our XPS analysis confirms the successful fabrication of an MAPbI$_3$/MXene heterostructured thin film.

Using the UPS technique, we investigate the electronic structure of the MAPbI$_3$/MXene heterostructure. First, we analysed the SECO region of F-MXene and N-MXene without perovskite addition, as presented in Fig. 3(a). We found that the extracted WF of F-MXene deposited on SiO$_2$ and Au are 3.62 and 3.68 eV, respectively. The WF of both samples only shows slight shifting between each other, which is still in the

experimental error range of the measurement. Furthermore, WFs of N-MXene on SiO$_2$ and Au are estimated to be 4.22 and 4.30 eV. Here, we notice a slight shift (0.08 eV) in the WF of N-MXene when different substrates were used. Based on the previous studies, the variation of the WF value can be attributed to the interface dipole and band bending effect at the film/substrate interface,[44,45] and functional groups present on the MXene surface.[8] However, in our case, the former can be neglected, considering the probing depth of UPS is about 2–3 nm[46] and our films have a thickness of 2 μm. Based on the study by Tamulewicz et al. the substrate effects on WF become important when we go down to the single or few-layer scale.[47] Thus, we can conclude that there is a variation in surface functional groups present in N-MXene grown on Au and SiO$_2$ substrates, leading to a slight difference in WF.

It is important to note that the WF of Ti$_3$C$_2$T$_x$ MXene strongly depends on the surface functional groups determined by the synthesis procedure.[8,12] Based on the DFT result, the calculated WF of bare Ti$_3$C$_2$ is 5.05 eV.[48] Moreover, the UPS determined WF of Ti$_3$C$_2$T$_x$ obtained by HF etching, as reported in different works is 4.42 eV[49] and 4.90 eV.[50] Thus, the WF of our N-MXene and F-MXene thin films are relatively low compared to the previously calculated WF of Ti$_3$C$_2$T$_x$, implying that
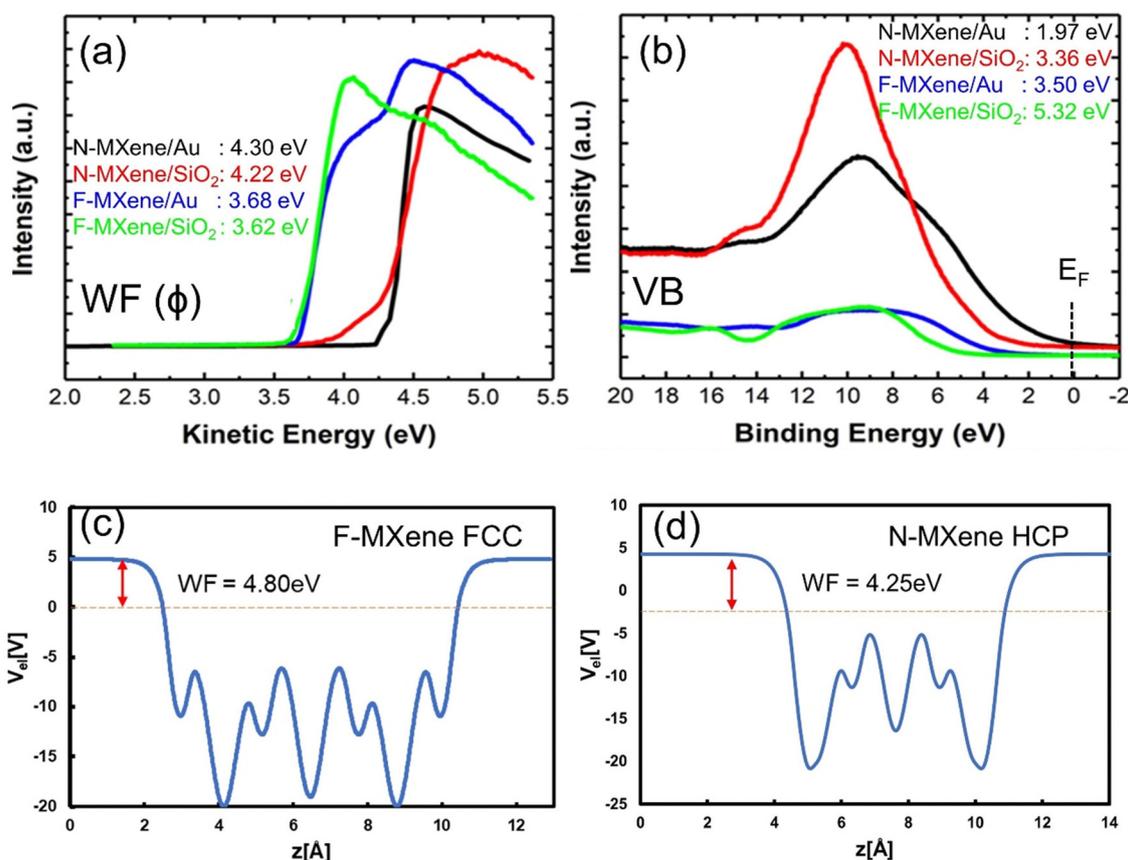

Fig. 3 (a) Secondary electron cut-off (SECO) signals of N-MXenes on Au (black) and SiO$_2$ (red), F-MXenes on Au (blue), and SiO$_2$ (green). The extracted work functions (WFs) are presented in the inset. (b) The valence band spectra of MXenes were recorded in various substrates and their corresponding extracted valence band maxima are shown in the inset. (c) Plane averaged electrostatic potential of F-MXene face-centred cubic (FCC) and (d) N-MXene hexagonal closed-packed (HCP) (zero referenced as the Fermi energy).

33086 | *Phys. Chem. Chem. Phys.*, 2023, **25**, 33081–33093

This journal is © the Owner Societies 2023

F and N atoms may act as n-dopants in the $Ti_3C_2T_x$ structure. Next, we analyse the valence band region of F-MXene and N-MXene, as depicted in Fig. 3(b). The spectra show the intensity starting from the Fermi energy and peaking at a binding energy value of around 10 eV. It is worth noting that in the case of F-MXene, the intensity is relaxed compared to N-MXene.

To provide a theoretical basis for our experimental findings, we performed density functional theory (DFT) calculations to investigate the electronic structure of F-MXene and N-MXene. The average electrostatic potential was calculated to determine the WF of MXene, with fluorine and nitrogen atoms positioned in different adsorption sites, i.e., bridge, FCC, HCP, and top sites.[8] From our UPS results, the WF of F-MXene is between 3.62 and 3.68 eV. The WF is smaller compared to the result obtained from DFT with the most stable configuration being fluorine atoms adsorbed on the FCC site with a value of 4.80 eV (Fig. 3(c) and Table S2, ESI†). Surprisingly, other adsorption sites give higher WFs of 4.80, 4.04, and 8.34 eV for bridge, HCP, and top sites, respectively (Fig. S15, ESI†). It is important to note that based on our XPS results, F-MXene is also terminated by a minor contribution from –OH groups. Therefore, such a low WF of F-MXene, as determined by UPS can be attributed to the co-existence of –OH groups on the MXene surface. To prove this hypothesis, we calculate the WF of –OH terminated $Ti_3C_2T_x$ MXene at different adsorption sites (Fig. S16, ESI†). Here, all of the –OH terminated MXene exhibit a low WF ranging from 1.87 to 2.55 eV, implying the contribution of –OH termination in lowering the WF of F-MXene.

For N-MXene, the theoretical WF obtained for the HCP site is 4.25 eV (Fig. 3(d)), which is consistent with the experimental value obtained by UPS analysis i.e., 4.22 eV (N-MXene on SiO_2) and 4.30 (N-MXene on Au). The HCP adsorption site is the most energetically favourable site for N adsorption (Table S3, ESI†). The previous result shows that MXene contains up to $\sim$30 at% of oxygen in the carbon layers, which is inherited from the MAX phase due to its decomposition/selective oxidation.[51–53] Thus, the good agreement between our DFT and experimental results indicates the high quality of synthesized F-MXene and N-MXene, without major contribution from oxygen incorporation in the MXene crystal structure (oxycarbides) and its oxidized species counterpart. Interestingly, we observe a considerable WF-increasing trend for other nitrogen adsorption sites, reaching 7.73, 7.66, and 9.02 eV, for bridge, FCC, and top sites, respectively (Fig. S17, ESI†). This variation can be explained by the difference in the density of electronic states available at the Fermi level, as we will explain later. The details of WF evolution in F-MXene and N-MXene are summarised in Table S4 (ESI†). Based on experimental and simulation results, introducing fluorine on the MXene surface yields a relatively low MXene WF, while nitrogen termination has the opposite role in obtaining a high WF. These findings demonstrate the potential for tuning the WF of MXene through the doping process, which is important for optoelectronic applications.

In addition to WF calculation, we also performed a theoretical investigation on the density of states (DOS) and partial density of states (PDOS) of F-MXene and N-MXene. Specifically, we calculated the DOS and PDOS for different adsorption sites of fluorine and nitrogen atoms on MXenes. Fig. S16a (ESI†) shows the DOS and PDOS of F-MXene with varying fluorine atom adsorption sites, i.e., bridge, FCC, HCP, and top sites. We found that all the adsorption configurations exhibited metallic behaviour, with the Fermi energy being filled with Ti 3d states. The valence band of the bridge, FCC, and HCP F-MXene arose from hybridization between F 2p and Ti 3d states. While in the top F-MXene site, we observed a different band structure characteristic with the valence band around −4 eV originating from F 2p states.

Next, we calculated the DOS and PDOS of N-MXene with different adsorption sites, as presented in Fig. S16b (ESI†). Here, we can see that incorporating nitrogen atoms on the MXene surface makes the electronic states at the Fermi energy much higher than F-MXene. However, in the case of N-MXene with the HCP site, the total electronic states at the Fermi energy are lower than at other sites. Unlike F-MXene, the Fermi energy of N-MXene resulted from N 2p, C 2p, and Ti 3d hybridization, suggesting the orbital hybridization between nitrogen, carbon, and titanium atoms plays a significant role in the electronic structure (Fig. 4(a) and (b)). This is happening due to the presence of a covalent bond between the C atom in Ti_3C_2 and the adsorbed N on the HCP site (Fig. 4(d)), which is not present in the F-MXene (F adsorbed on FCC site) counterpart (Fig. 4(c)). To further support this argument, we plot the electron localization function (ELF), which can be used to characterize the bonding behaviour[54] of N-MXene shown in Fig. S19 (ESI†). The ELF shows the presence of a C–N covalent bond in N-MXene (HCP).

Besides revealing the influence of nitrogen terminations on the electronic band structure, we also calculated the theoretical WF of $Ti_3C_2T_x$ MXene when a nitrogen atom replaces a carbon site (Fig. 5). This calculation is essential as Ti 2p and N 1s XPS spectra of N-MXene indicate the formation of a Ti–N bond. In this calculation, we used –OH terminated MXene at HCP sites and –F terminated MXene at FCC sites, as these configurations are the most energetically favourable for nitrogen doping. In addition, –F and –OH termination are the main terminations observed in the N-MXene sample, as revealed by O 1s XPS spectra. Here, –OH terminated MXene shows an ultralow WF of 2.42 eV (Fig. 5(a)). On the other hand, F-terminated MXene exhibits a large WF of 4.80 eV (Fig. 5(b)).

Next, we replaced one of the carbon atoms in the $Ti_3C_2T_x$ lattice with one nitrogen atom. Notably, by performing nitrogen doping, –OH terminated MXene at HCP sites (Fig. 5(c)) underwent a lowering of WF from 2.42 to 2.09 eV. In the case of –F terminated MXene at FCC sites (Fig. 5(d)), WF lowers from 4.80 to 4.69 eV. Thus, we observed a similar decreasing WF trend for both configurations when introducing a nitrogen atom to the lattice. This finding is quite different when nitrogen atoms terminate the MXene surface, in which WF can reach up to 9 eV. Therefore, we argued that the low WF experimental value of N-MXene (4.30 eV for N-MXene on Au and 4.22 for N-MXene on SiO_2) could also be caused by nitrogen atom that occupied

This journal is © the Owner Societies 2023

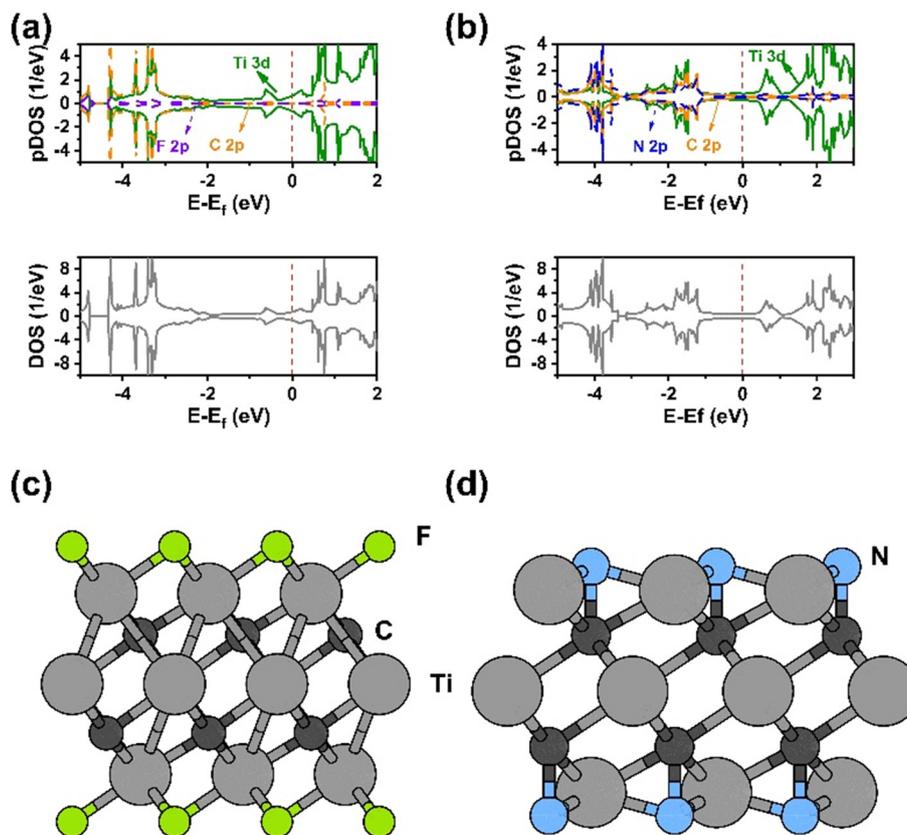Phys. Chem. Chem. Phys., 2023, 25, 33081–33093 | 33087

Fig. 4 Partial (PDOS), total density of states (DOS) of (a) F-MXene with the F atom adsorbed in the FCC site and (b) N-MXene with the N atom adsorbed in the HCP site. Optimized structure of (c) F-MXene with the F atom adsorbed in the FCC site and (d) N-MXene with the N atom adsorbed in the HCP site.
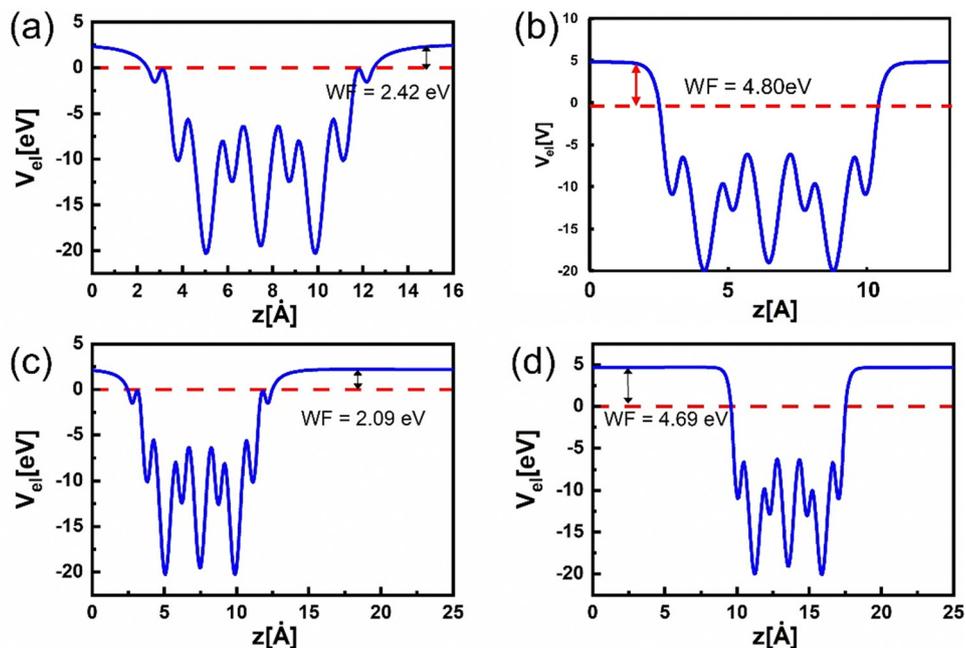

Fig. 5 Plane averaged electronic potential *vs.* z for (a) −OH terminated MXene at HCP sites. (b) −F terminated MXene at FCC sites. (c) N-doped −OH HCP terminated MXene. (d) N-doped FCC −F terminated MXene. Here, nitrogen doping is performed by replacing one of the carbon atoms in the $Ti_3C_2T_x$ lattice. −OH HCP and −F FCC termination sites were chosen as these configurations are energetically favourable for performing nitrogen doping.

the carbon lattice of MXene structure partially by forming Ti–N bond as supported by XPS analysis.

Fig. S20a–d (ESI†) displays the PDOS and DOS of N-MXene, where nitrogen replaces one carbon atom. First, by comparing the electronic states between –OH terminated and –F terminated MXene, it becomes clear that –OH termination gives more electronic states at the Fermi level compared to –F terminated MXene. In particular, –OH terminated MXene shows the majority of Ti 3d states at the Fermi level with a weak contribution of C 2p, O 2p, and H 1s hybridizations (Fig. S20a, ESI†). In the case of –F terminated MXene (Fig. S20b, ESI†), we only observe Ti 3d states at the Fermi level.

After we discussed the electronic structures of F-MXene and N-MXene, we moved to the electronic structure of $MAPbI_3$ grown on Au and SiO_2 substrates. The measured SECO region of perovskite samples is presented in Fig. S21 (ESI†). We can see that the secondary electron offset of the spectra gave WF of 4.09 eV and 4.52 eV for $MAPbI_3$ on Au and SiO_2, respectively. The differences in these values can be attributed to the different chemical natures of the samples. Previous theoretical studies revealed that the WF of $MAPbI_3$ can be tuned between 4.00 and 4.80 eV for PbI_2 rich and MAI rich, respectively.[55]

Next, we study the MXene WF changes upon the fabrication of $MAPbI_3$/MXene heterostructured thin film. The WF estimated by the SECO is presented in Fig. 6(a). By introducing N-MXene into the targeted hybrid perovskite structure, we see that $MAPbI_3$ exhibited a slightly lower WF, *i.e.*, 4.45 eV and 4.35 eV for N-MXene/$MAPbI_3$ grown on Au and SiO_2, respectively. Interestingly, a dramatic lowering of WF is observed when $MAPbI_3$ is combined with F-MXene. $MAPbI_3$/F-MXene grown on Au and SiO_2 show WF of 3.00 and 3.45 eV, respectively. Our results suggest that N-MXene and F-MXene act as an n-dopant, which upshifts the Fermi energy of the perovskite towards the vacuum level. In this case, a robust interfacial connection of MXene/perovskite is established, in which electrons are transferred from low-work function MXene to the perovskite layers and induce the interface dipole.[2] A similar mechanism has been experimentally observed in N-doped graphene quantum dot/$MAPbI_3$.[56] To determine the valence band maximum (VBM) of

$MAPbI_3$ thin film, the UPS valence band region is presented in Fig. 6(b). The VBM of N-MXene/$MAPbI_3$ thin film deposited on Au and SiO_2 are 3.50 and 7.62 eV, respectively. Moreover, in F-MXene/$MAPbI_3$, the VBM value is estimated to be 5.12 eV (on Au) and 3.45 eV (on SiO_2). Table S5 (ESI†) summarised the WF and VBM changes of $MAPbI_3$/MXene heterostructure on Au and SiO_2 substrates.

We further investigate the optical properties of F-MXene, N-MXene, and $MAPbI_3$/MXene heterostructured thin film *via* PL measurements. Fig. 7(a) reveals that F-MXene and N-MXene exhibit relatively weak PL signals with peaks at 450 and 400 nm, respectively.[57] From our DOS results, F-MXene and N-MXene are good conductors owing to their rich electronic states at the Fermi level. Thus, the weak observed PL signal does not originate from $Ti_3C_2T_x$ flakes. The observed PL emission of the samples corresponds to TiO_2 species on the surface,[57] as we detected TiO_2 and $TiO_{2-x}F_x$ in both F-MXene and N-MXene in Ti 2p XPS spectra. Furthermore, the slight difference in the PL peak position of N-MXene and F-MXene may be due to different native defects present in the TiO_2 lattice.[57,58]

To further investigate the PL properties of $MAPbI_3$/MXene heterostructure in detail, we also examined the PL response of bare $MAPbI_3$ films. Under 532 nm laser excitation, a strong PL intensity with a broad peak was observed at 766 nm for the corresponding films (Fig. 7(b)), which agrees with the previous reports.[59,60] Moreover, we find that the PL intensity of $MAPbI_3$ deposition on Au is lower than on SiO_2, possibly due to factors such as non-radiative recombination centres, variation in film thickness, and crystal quality.[61,62] Upon the formation of $MAPbI_3$/MXene heterostructure, the PL is strongly quenched, which might be attributed to the n-doping or charge transfer effect between MXene and perovskite at the interface.[63,64] Additionally, PL quenching is an indicator of excellent interfacial contact in metal/semiconductor heterostructure.[65] We measured TR-PL decay curves to further explore the charge carrier dynamics in MXene thin films (Fig. 7(c)). Both N-MXene and F-MXene exhibited a rapid decay, which might be attributed to the charge transfer from light-active TiO_2 to $Ti_3C_2T_x$ through a Schottky interface. TR-PL spectra of $MAPbI_3$ on SiO_2
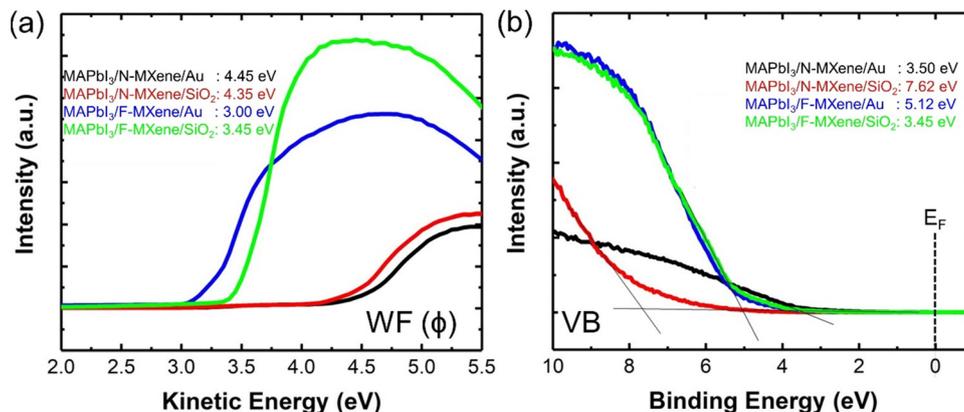

Fig. 6 The spectral evolution of MXenes upon $MAPbI_3$ doping. (a) The respective values are shown as indicated in the SECO region and (b) the valence band region where the valence band maximum (VBM) is acquired at the interpolation from the spectral edge to the baseline.

This journal is © the Owner Societies 2023

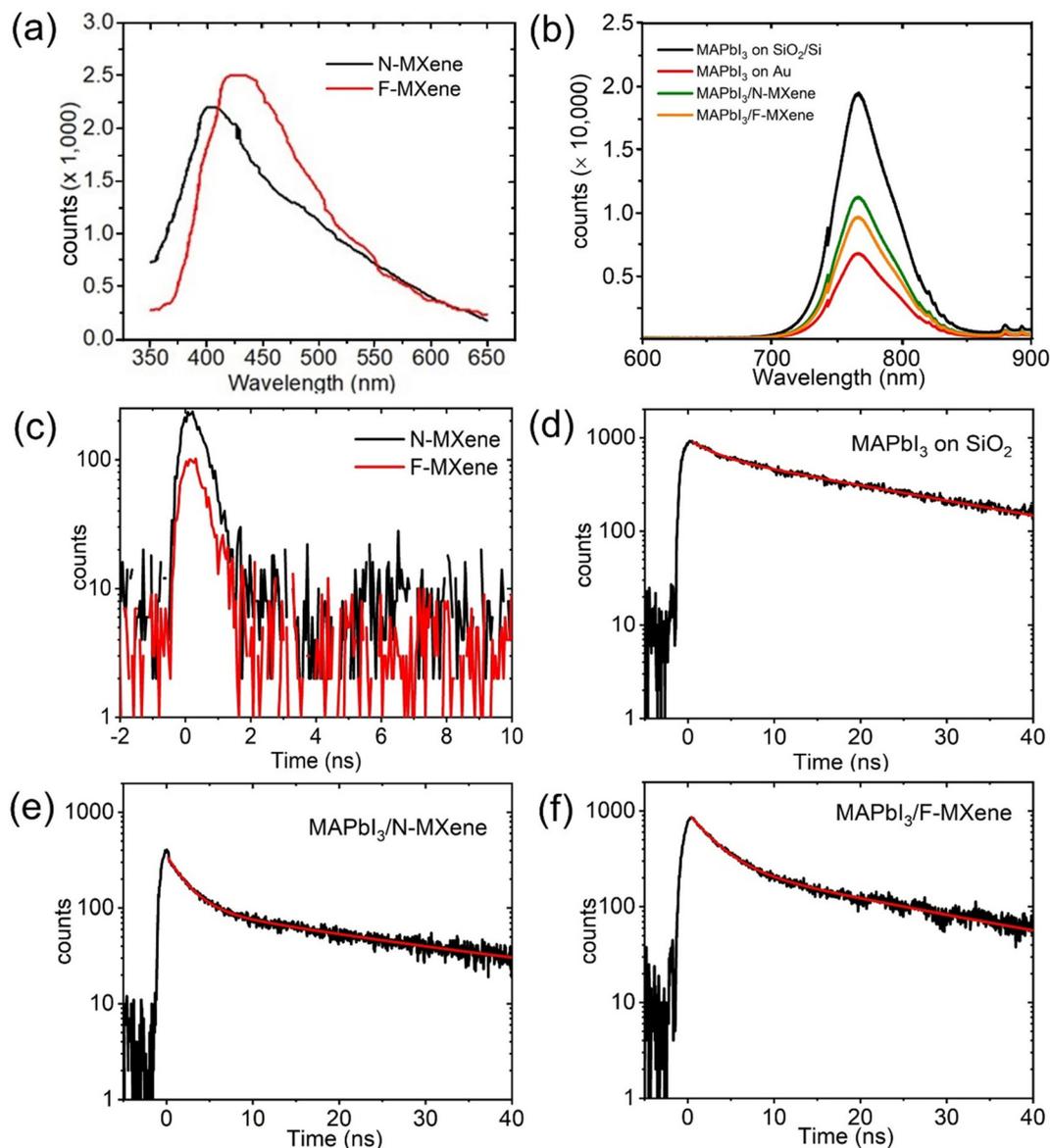*Phys. Chem. Chem. Phys.*, 2023, **25**, 33081–33093 | **33089**

Fig. 7 Optical properties of N-MXenes and F-MXenes and their interactions with MAPbI₃. (a) Steady-state photoluminescence (PL) spectra of pristine MXenes samples. (b) PL spectra of MAPbI₃/MXenes heterostructure. Time-resolved PL (TR-PL) decay curve of (c) N- and F-MXenes, (d) MAPbI₃ on SiO₂, (e) MAPbI₃ on N-MXenes, and (f) MAPbI₃ on F-MXenes. (a) and (c) were obtained with excitation at 266 nm, while (b), (d), (e), and (f) were at 532 nm. Decay curve of (b) for 450 nm emission while those of (d), (e), (f) for emission beyond 650 nm.

thin film are presented in Fig. 7(d). The decay curve is fitted by two components (Table 1). The first decay (2.9 ns) is attributed to the emission from the self-trapped excitons, whereas the second decay (26 ns) is related to the emission from the recombination of free carriers.[66] The average decay time of MAPbI₃ on SiO₂ is calculated to be 16.6 ns.

Next, we investigate the decay profile of MAPbI₃/MXene heterostructure thin films, which has shown promising potential in tuning the performance of perovskite-based optoelectronic devices. As illustrated in Fig. 7(e), TR-PL spectra of MAPbI₃/N-MXene reveal a decreased average decay time of 14.2 ns, compared to pristine MAPbI₃, with a decay time of 16.6 ns. Introducing F-MXene in the heterostructure (Fig. 7(f))

Table 1 Extracted parameters from the fitting of TRPL curves

Sample	τ_1 (ns)	A_1 (%)	τ_2 (ns)	A_2 (%)	τ_{avg} (ns)
MAPbI₃ on SiO₂	2.9	5	26.0	95	16.6
MAPbI₃/N-MXene	2.2	23	26.4	77	14.2
MAPbI₃/F-MXene	3.0	24	23.8	76	12.5

further decreased the decay time to an average lifetime of 12.5 ns. This faster carrier lifetime in MAPbI₃/F-MXene, as compared to MAPbI₃/N-MXene, can be attributed to the more efficient charge transfer pathway provided by F-MXene, resulting in more substantial PL quenching. The different PL quenching is connected to different doped-MXene/perovskite

33090 | Phys. Chem. Chem. Phys., 2023, 25, 33081–33093

This journal is © the Owner Societies 2023

heterostructure interfacial properties. Previously, Tao *et al.* demonstrated that the charge transfer ability of $Ti_3C_2T_x$ can be controlled by introducing different types of surface functional groups.[67] They constructed $WS_2/Ti_3C_2T_x$ heterostructure and showed that F-MXene has more efficient charge transfer than N-MXene. Thus, our findings demonstrate the potential of F-MXene to tune the electronic structure of perovskite-based optoelectronic devices effectively.

4. Conclusion

This study presents a comprehensive interfacial engineering of the optoelectronic properties of $Ti_3C_2T_x$ MXene/MAPbI$_3$ heterostructures by tuning the WF of MAPbI$_3$. We elucidated the chemical states of $Ti_3C_2T_x$ of respective fluorine termination (F-MXene) and nitrogen doping (N-MXene) by the XPS technique. Fluorine atoms decorated the outermost surface of F-MXene, while nitrogen atoms were partially adsorbed on the N-MXene surface and doped the crystal lattice.

The UPS spectra have shown that the F-termination and N-doping of $Ti_3C_2T_x$ yield low WFs ranging from 3.34 to 4.30 eV. These experimental results are comparable with DFT results, considering four adsorption sites of the respective atoms (hexagonal closed-packed, face-centred cubic, bridge, and top sites). MXene/MAPbI$_3$ heterostructures constructed from F-terminated and N-doped MXenes further result in WF tuning of MAPbI$_3$ within 3.00–4.45 eV. Due to the efficient charge transfer pathway, strong PL quenching and faster average decay time were observed for both heterostructures compared to pristine counterparts.

Altogether, our results show excellent MXene/MAPbI$_3$ heterostructure tunability regarding WF and optical properties by surface termination and non-metal elemental doping. The obtained results formulate an essential step for tailoring the interfacial electronic structure of MXenes toward optoelectronic applications.

Author contributions

MAKP: investigation, formal analysis, data curation, visualization, and writing – original draft. A: conceptualization, methodology, data curation, resources, supervision, and writing – review & editing. SWK: investigation and validation. FM: investigation and validation. DM: investigation. JM: investigation, formal analysis, visualization, and writing – review & editing. YD: investigation, resources, and writing – review & editing. DK: investigation and writing – review & editing. HL: resources and supervision. MDB: resources, project administration, conceptualization, writing – review & editing, and supervision. AMJ: supervision and writing – review & editing.

Conflicts of interest

There are no conflicts of interest to declare.

References

1 M. L. Agiorgousis, Y.-Y. Sun, H. Zeng and S. Zhang, Strong Covalency-Induced Recombination Centers in Perovskite Solar Cell Material CH$_3$NH$_3$PbI$_3$, *J. Am. Chem. Soc.*, 2014, **136**, 14570–14575.

2 A. Di Vito, A. Pecchia, M. Auf der Maur and A. Di Carlo, Nonlinear work function tuning of lead-halide perovskites by MXenes with mixed terminations, *Adv. Funct. Mater.*, 2020, **30**, 1909028.

3 M. Naguib, M. Kurtoglu, V. Presser, J. Lu, J. Niu, M. Heon, L. Hultman, Y. Gogotsi and M. W. Barsoum, Two-dimensional nanocrystals produced by exfoliation of Ti$_3$AlC$_2$, *Adv. Mater.*, 2011, **23**, 4248–4253.

4 S. Abdolhosseinzadeh, X. Jiang, H. Zhang, J. Qiu and C. J. Zhang, Perspectives on solution processing of two-dimensional MXenes, *Mater. Today*, 2021, **48**, 214–240.

5 A. S. Zeraati, S. A. Mirkhani, P. Sun, M. Naguib, P. V. Braun and U. Sundararaj, Improved synthesis of $Ti_3C_2T_x$ MXenes resulting in exceptional electrical conductivity, high synthesis yield, and enhanced capacitance, *Nanoscale*, 2021, **13**, 3572–3580.

6 A. D. Dillon, M. J. Ghidiu, A. L. Krick, J. Griggs, S. J. May, Y. Gogotsi, M. W. Barsoum and A. T. Fafarman, Highly conductive optical quality solution-processed films of 2D titanium carbide, *Adv. Funct. Mater.*, 2016, **26**, 4162–4168.

7 M. Khazaei, M. Arai, T. Sasaki, C. Chung, N. S. Venkataramanan, M. Estili, Y. Sakka and Y. Kawazoe, Novel electronic and magnetic properties of two-dimensional transition metal carbides and nitrides, *Adv. Funct. Mater.*, 2013, **23**, 2185–2192.

8 T. Schultz, N. C. Frey, K. Hantanasirisakul, S. Park, S. J. May, V. B. Shenoy, Y. Gogotsi and N. Koch, Surface termination dependent work function and electronic properties of $Ti_3C_2T_x$ MXene, *Chem. Mater.*, 2019, **31**, 6590–6597.

9 H. Jing, H. Yeo, B. Lyu, J. Ryou, S. Choi, J.-H. Park, B. H. Lee, Y.-H. Kim and S. Lee, Modulation of the electronic properties of MXene ($Ti_3C_2T_x$) via surface-covalent functionalization with diazonium, *ACS Nano*, 2021, **15**, 1388–1396.

10 Y. Liu, H. Xiao and W. A. Goddard III, Schottky-barrier-free contacts with two-dimensional semiconductors by surface-engineered MXenes, *J. Am. Chem. Soc.*, 2016, **138**, 15853–15856.

11 M. Khazaei, M. Arai, T. Sasaki, A. Ranjbar, Y. Liang and S. Yunoki, OH-terminated two-dimensional transition metal carbides and nitrides as ultralow work function materials, *Phys. Rev. B: Condens. Matter Mater. Phys.*, 2015, **92**, 075411.

This journal is © the Owner Societies 2023

Phys. Chem. Chem. Phys., 2023, **25**, 33081–33093 | **33091**

12 A. Agresti, A. Pazniak, S. Pescetelli, A. Di Vito, D. Rossi, A. Pecchia, M. Auf der Maur, A. Liedl, R. Larciprete and D. V. Kuznetsov, Titanium-carbide MXenes for work function and interface engineering in perovskite solar cells, *Nat. Mater.*, 2019, **18**, 1228–1234.

13 Z. Zhong and P. Hansmann, Tuning the work function in transition metal oxides and their heterostructures, *Phys. Rev. B*, 2016, **93**, 235116.

14 A. M. Al-Amri, B. Cheng and J.-H. He, Perovskite methylammonium lead trihalide heterostructures: progress and challenges, *IEEE Trans. Nanotechnol.*, 2018, **18**, 1–12.

15 Y. Bao, Y. Liu, J. Pan, P. Chen, X. Liu, Y. Li, X. Tang, W. Zhang, B. Liu and J. Liu, Constructing 2D layered PCN/Ti_3C_2/Bi_2MoO_6 heterojunction with MXene as charge mediator for enhanced photocatalytic performance, *Appl. Surf. Sci.*, 2022, **589**, 152883.

16 J. Zhu, H. Wang, L. Ma and G. Zou, Observation of ambipolar photoresponse from 2D MoS_2/MXene heterostructure, *Nano Res.*, 2021, **14**, 3416–3422.

17 M. A. K. Purbayanto, M. Chandel, M. Birowska, A. Rosenkranz and A. M. Jastrzębska, Optically Active MXenes in van der Waals Heterostructures, *Adv. Mater.*, 2023, 2301850.

18 M. A. K. Purbayanto, D. Bury, M. Chandel, Z. D. Shahrak, V. N. Mochalin, A. Wójcik, D. Moszczyńska, A. Wojciechowska, A. Tabassum, M. Naguib and A. M. Jastrzębska, Ambient Processed rGO/Ti_3CNT_x MXene Thin Film with High Oxidation Stability, Photosensitivity, and Self-Cleaning Potential, *ACS Appl. Mater. Interfaces*, 2023, **15**, 44075–44086.

19 A. S. Bati, A. A. Sutanto, M. Hao, M. Batmunkh, Y. Yamauchi, L. Wang, Y. Wang, M. K. Nazeeruddin and J. G. Shapter, Cesium-doped $Ti_3C_2T_x$ MXene for efficient and thermally stable perovskite solar cells, *Cell Rep. Phys. Sci.*, 2021, **2**, 100598.

20 Z. Guo, L. Gao, Z. Xu, S. Teo, C. Zhang, Y. Kamata, S. Hayase and T. Ma, High electrical conductivity 2D MXene serves as additive of perovskite for efficient solar cells, *Small*, 2018, **14**, 1802738.

21 Z. Guo, J. Zhou and Z. Sun, New two-dimensional transition metal borides for Li ion batteries and electrocatalysis, *J. Mater. Chem. A*, 2017, **5**, 23530–23535.

22 S. Wei, S. Tie, K. Shen, H. Sun, X. Zheng, H. Wang, W. Liang, J. Zou, Y. Huang and L. Luo, Enhanced Carrier Transport in X-Ray Detector Based on $Cs_3Bi_2I_9$/MXene Composite Wafers, *Adv. Opt. Mater.*, 2022, **10**, 2201585.

23 C. Lu, L. Yang, B. Yan, L. Sun, P. Zhang, W. Zhang and Z. Sun, Nitrogen-doped Ti_3C_2 MXene: mechanism investigation and electrochemical analysis, *Adv. Funct. Mater.*, 2020, **30**, 2000852.

24 R. Wang, M. Li, K. Sun, Y. Zhang, J. Li and W. Bao, Element-Doped Mxenes: Mechanism, Synthesis, and Applications, *Small*, 2022, **18**, 2201740.

25 Y. Wen, T. E. Rufford, X. Chen, N. Li, M. Lyu, L. Dai and L. Wang, Nitrogen-doped $Ti_3C_2T_x$ MXene electrodes for high-performance supercapacitors, *Nano Energy*, 2017, **38**, 368–376.

26 L. Pu, J. Zhang, N. K. L. Jiresse, Y. Gao, H. Zhou, N. Naik, P. Gao and Z. Guo, N-doped MXene derived from chitosan for the highly effective electrochemical properties as super-capacitor, *Adv. Compos. Hybrid Mater.*, 2022, 1–14.

27 W. Xu, S. Li, W. Zhang, B. Ouyang, W. Yu and Y. Zhou, Nitrogen-Doped $Ti_3C_2T_x$ MXene Induced by Plasma Treatment with Enhanced Microwave Absorption Properties, *ACS Appl. Mater. Interfaces*, 2021, **13**, 49242–49253.

28 L. Tjahjana, A. Olivier, Y. Herbani, H. Hardhienata, F. Ahmad, Arramel, D. Kowal, M. D. Birowosuto and H. Wang, Localized Visible Wavelength Photoluminescence from GaP/InP Heterostructure Nanowires, *J. Phys. Chem. C*, 2022, **126**, 12113–12120.

29 P. Giannozzi, S. Baroni, N. Bonini, M. Calandra, R. Car, C. Cavazzoni, D. Ceresoli, G. L. Chiarotti, M. Cococcioni and I. Dabo, QUANTUM ESPRESSO: a modular and open-source software project for quantum simulations of materials, *J. Phys.: Condens. Matter*, 2009, **21**, 395502.

30 J. P. Perdew and A. Zunger, Self-interaction correction to density-functional approximations for many-electron systems, *Phys. Rev. B: Condens. Matter Mater. Phys.*, 1981, **23**, 5048.

31 Y. Li, H. Shao, Z. Lin, J. Lu, L. Liu, B. Duployer, P. O. Persson, P. Eklund, L. Hultman and M. Li, A general Lewis acidic etching route for preparing MXenes with enhanced electrochemical performance in non-aqueous electrolyte, *Nat. Mater.*, 2020, **19**, 894–899.

32 M. Naguib, V. N. Mochalin, M. W. Barsoum and Y. Gogotsi, 25th anniversary article: MXenes: a new family of two-dimensional materials, *Adv. Mater.*, 2014, **26**, 992–1005.

33 K. Liang, A. Tabassum, A. Majed, C. Dun, F. Yang, J. Guo, K. Prenger, J. J. Urban and M. Naguib, Synthesis of new two-dimensional titanium carbonitride $Ti_2C_{0.5}N_{0.5}T_x$ MXene and its performance as an electrode material for sodium-ion battery, *InfoMat*, 2021, **3**, 1422–1430.

34 E. B. Deeva, A. Kurlov, P. M. Abdala, D. Lebedev, S. M. Kim, C. P. Gordon, A. Tsoukalou, A. Fedorov and C. R. Müller, In Situ XANES/XRD Study of the Structural Stability of Two-Dimensional Molybdenum Carbide Mo_2CT_x: Implications for the Catalytic Activity in the Water–Gas Shift Reaction, *Chem. Mater.*, 2019, **31**, 4505–4513.

35 J. Halim, K. M. Cook, M. Naguib, P. Eklund, Y. Gogotsi, J. Rosen and M. W. Barsoum, X-ray photoelectron spectroscopy of select multi-layered transition metal carbides (MXenes), *Appl. Surf. Sci.*, 2016, **362**, 406–417.

36 J. D. Gouveia and J. R. B. Gomes, The determining role of Tx species in the catalytic potential of MXenes: Water adsorption and dissociation on Mo_2CT_x, *Catal. Today*, 2023, **424**, 113848.

37 V. Natu, M. Benchakar, C. Canaff, A. Habrioux, S. Celerier and M. W. Barsoum, A critical analysis of the X-ray photoelectron spectra of $Ti_3C_2T_z$ MXenes, *Matter*, 2021, **4**, 1224–1251.

38 L. Yu, Z. Fan, Y. Shao, Z. Tian, J. Sun and Z. Liu, Versatile N-doped MXene ink for printed electrochemical energy storage application, *Adv. Energy Mater.*, 2019, **9**, 1901839.

39 Y. Tang, J. Zhu, W. Wu, C. Yang, W. Lv and F. Wang, Synthesis of nitrogen-doped two-dimensional Ti_3C_2 with enhanced electrochemical performance, *J. Electrochem. Soc.*, 2017, **164**, A923.

40 S.-Y. Liao, S.-F. Cui, Y.-Z. Li, W.-X. Cheng, X.-W. Huang, J. Zhang, T.-T. Cui, X.-G. Shu and Y.-G. Min, Wrinkled and

33092 | *Phys. Chem. Chem. Phys.*, 2023, **25**, 33081–33093

This journal is © the Owner Societies 2023

flexible N-doped MXene additive for improving the mechanical and electrochemical properties of the nickel-rich LiNi$_{0.8}$-Co$_{0.1}$Mn$_{0.1}$O$_2$ cathode, *Electrochim. Acta*, 2022, **410**, 139989.

41 C. Rocks, V. Svrcek, P. Maguire and D. Mariotti, Understanding surface chemistry during MAPbI$_3$ spray deposition and its effect on photovoltaic performance, *J. Mater. Chem. C*, 2017, **5**, 902–916.

42 H. Xie, X. Liu, L. Lyu, D. Niu, Q. Wang, J. Huang and Y. Gao, Effects of precursor ratios and annealing on electronic structure and surface composition of CH$_3$NH$_3$PbI$_3$ perovskite films, *J. Phys. Chem. C*, 2016, **120**, 215–220.

43 Z. Shao, S. You, X. Guo, J. Xiao, J. Liu, F. Song, H. Xie, J. Sun and H. Huang, Temperature-dependent photoluminescence of Co-evaporated MAPbI$_3$ ultrathin films, *Results Phys.*, 2022, **34**, 105326.

44 S. Olthof and K. Meerholz, Substrate-dependent electronic structure and film formation of MAPbI$_3$ perovskites, *Sci. Rep.*, 2017, **7**, 40267.

45 F. Amy, C. Chan and A. Kahn, Polarization at the gold/pentacene interface, *Org. Electron.*, 2005, **6**, 85–91.

46 F. Zhang, S. H. Silver, N. K. Noel, F. Ullrich, B. P. Rand and A. Kahn, Ultraviolet photoemission spectroscopy and Kelvin probe measurements on metal halide perovskites: Advantages and pitfalls, *Adv. Energy Mater.*, 2020, **10**, 1903252.

47 M. Tamulewicz, J. Kutrowska-Girzycka, K. Gajewski, J. Serafińczuk, A. Sierakowski, J. Jadczak, L. Bryja and T. P. Gotszalk, Layer number dependence of the work function and optical properties of single and few layers MoS$_2$: effect of substrate, *Nanotechnology*, 2019, **30**, 245708.

48 Y. Liu, Y.-H. Li, X. Li, Q. Zhang, H. Yu, X. Peng and F. Peng, Regulating Electron–Hole Separation to Promote Photocatalytic H$_2$ Evolution Activity of Nanoconfined Ru/MXene/TiO$_2$ Catalysts, *ACS Nano*, 2020, **14**, 14181–14189.

49 P. Zhang, Y. Li, Y. Zhang, R. Hou, X. Zhang, C. Xue, S. Wang, B. Zhu, N. Li and G. Shao, Photogenerated Electron Transfer Process in Heterojunctions: In Situ Irradiation XPS, *Small Methods*, 2020, **4**, 2000214.

50 G. Ding, K. Zeng, K. Zhou, Z. Li, Y. Zhou, Y. Zhai, L. Zhou, X. Chen and S.-T. Han, Configurable multi-state nonvolatile memory behaviors in Ti$_3$C$_2$ nanosheets, *Nanoscale*, 2019, **11**, 7102–7110.

51 P. P. Michałowski, M. Anayee, T. S. Mathis, S. Kozdra, A. Wójcik, K. Hantanasirisakul, I. Jóźwik, A. Piątkowska, M. Możdżonek, A. Malinowska, R. Diduszko, E. Wierzbicka and Y. Gogotsi, Oxycarbide MXenes and MAX phases identification using monoatomic layer-by-layer analysis with ultralow-energy secondary-ion mass spectrometry, *Nat. Nanotechnol.*, 2022, **17**, 1192–1197.

52 G. M. Song, S. B. Li, C. X. Zhao, W. G. Sloof, S. van der Zwaag, Y. T. Pei and J. Th. M. De Hosson, Ultra-high temperature ablation behavior of Ti$_2$AlC ceramics under an oxyacetylene flame, *J. Eur. Ceram*, 2011, **31**, 855–862.

53 X. H. Wang and Y. C. Zhou, Stability and Selective Oxidation of Aluminum in Nano-Laminate Ti$_3$AlC$_2$ upon Heating in Argon, *Chem. Mater.*, 2003, **15**, 3716–3720.

54 J. Manopo, P. N. Kusumo, A. Sumboja and Y. Darma, Coordination engineering of atomically dispersed zirconium on graphene for the oxygen reduction reaction, *Phys. Chem. Chem. Phys.*, 2023, **25**, 25299–25308.

55 W.-J. Yin, T. Shi and Y. Yan, Unusual defect physics in CH$_3$NH$_3$PbI$_3$ perovskite solar cell absorber, *Appl. Phys. Lett.*, 2014, **104**, 063903.

56 X. Gan, S. Yang, J. Zhang, G. Wang, P. He, H. Sun, H. Yuan, L. Yu, G. Ding and Y. Zhu, Graphite-N doped graphene quantum dots as semiconductor additive in perovskite solar cells, *ACS Appl. Mater. Interfaces*, 2019, **11**, 37796–37803.

57 L. Zhang, W. Su, H. Shu, T. Lü, L. Fu, K. Song, X. Huang, J. Yu, C.-T. Lin and Y. Tang, Tuning the photoluminescence of large Ti$_2$C$_2$T$_x$ MXene flakes, *Ceram. Int.*, 2019, **45**, 11468–11474.

58 X. Sang, Y. Xie, M.-W. Lin, M. Alhabeb, K. L. Van Aken, Y. Gogotsi, P. R. C. Kent, K. Xiao and R. R. Unocic, Atomic Defects in Monolayer Titanium Carbide (Ti$_3$C$_2$T$_x$) MXene, *ACS Nano*, 2016, **10**, 9193–9200.

59 Q. Zhu, X. Bao, J. Yu, D. Zhu, M. Qiu, R. Yang and L. Dong, Compact layer free perovskite solar cells with a high-mobility hole-transporting layer, *ACS Appl. Mater. Interfaces*, 2016, **8**, 2652–2657.

60 A. F. Akbulatov, L. A. Frolova, S. A. Tsarev, I. Zhidkov, S. Y. Luchkin, E. Z. Kurmaev, K. J. Stevenson, S. M. Aldoshin and P. A. Troshin, Film deposition techniques impact the defect density and photostability of MAPbI$_3$ Perovskite films, *J. Phys. Chem. C*, 2020, **124**, 21378–21385.

61 S. Parveen, S. M. Obaidulla and P. Giri, Growth kinetics of hybrid perovskite thin films on different substrates at elevated temperature and its direct correlation with the microstructure and optical properties, *Appl. Surf. Sci.*, 2020, **530**, 147224.

62 Y. Xue, J. Yuan, J. Liu and S. Li, Controllable synthesis of 2D perovskite on different substrates and its application as photodetector, *Nanomaterials*, 2018, **8**, 591.

63 W. Li, F. Wang, Z. Zhang and S. Min, MAPbI$_3$ microcrystals integrated with Ti$_3$C$_2$T$_x$ MXene nanosheets for efficient visible-light photocatalytic H$_2$ evolution, *Chem. Commun.*, 2021, **57**, 7774–7777.

64 J. M. Bharathan and Y. Yang, Polymer/metal interfaces and the performance of polymer light-emitting diodes, *J. Appl. Phys.*, 1998, **84**, 3207–3211.

65 H. Tan, Y. Fan, Y. Rong, B. Porter, C. S. Lau, Y. Zhou, Z. He, S. Wang, H. Bhaskaran and J. H. Warner, Doping graphene transistors using vertical stacked monolayer WS$_2$ heterostructures grown by chemical vapor deposition, *ACS Appl. Mater. Interfaces*, 2016, **8**, 1644–1652.

66 K. J. Karki, M. Abdellah, W. Zhang and T. Pullerits, Different emissive states in the bulk and at the surface of methylammonium lead bromide perovskite revealed by two-photon micro-spectroscopy and lifetime measurements, *APL Photonics*, 2016, **1**, 046103.

67 Y. Tao, S. W. Koh, X. Yu, C. Wang, H. Liang, Y. Zhang, H. Li and Q. J. Wang, Surface group-modified MXene nano-flake doping of monolayer tungsten disulfides, *Nanoscale Adv.*, 2019, **1**, 4783–4789.

This journal is © the Owner Societies 2023

Phys. Chem. Chem. Phys., 2023, **25**, 33081–33093 | **33093**